Communication

Multiphase-Field Modeling of Micropore Formation in Metallic Alloys

HOSSEIN MEIDANI, ALAIN JACOT, and MICHEL RAPPAZ

A 3D phase-field (PhF) model has been developed to study the formation of micropores constrained to grow within a well-developed solid network. The model accounts for the equilibrium condition at triple (solid–liquid–pore) lines and the partitioning of dissolved gases. Growth of a micropore in a representative volume element taken from X-ray tomography was simulated, which offered the possibility to study the pore evolution in temporal and spatial resolutions that are not possible in experiments.

DOI: 10.1007/s11661-014-2647-9

Formation of defects such as microporosity limits the mechanical properties of cast parts. They are induced by both solidification shrinkage and gas segregation that occur concomitantly during the solidification, in the mushy zone.[1]

Most advanced models of microporosity formation solve at the scale of the process average conservation equations for the evolution of the solid fraction, the flow of interdendritic liquid, and the partitioning and diffusion of gases during solidification.[2–7] During its growth, the pressure inside the pore exceeds that of the surrounding liquid due to capillarity forces between liquid and gas. Therefore, to close the problem mathematically, a so-called *pinching model*, *i.e.*, a mathematical expression relating the radius of curvature of the pore–liquid interface to a microstructural parameter (*e.g.*, solid fraction) is required.[3,7–9] For a spherical pore, this relationship is straightforward; however, in reality, due to numerous contacts with the solid phase, pores take a complex and highly tortuous shape. Local mean curvatures as high as 0.2 μm^{-1} have been measured in aluminum alloys by X-ray tomography (XRT), which correspond to overpressures as high as 400 kPa in the pore with respect to the surrounding liquid,[10] that can directly affect the pore size and fraction.

Different pinching models have been proposed which all share simplifications of the pore shape[3,7–9]; still, these assumptions are not backed with an extensive study of the pore morphology. To address this issue, Felberbaum and Rappaz performed XRT observations and studied pores in solidified Al-Cu alloys.[10] Curvature distribution on the pore–liquid interface is of interest since it plays an important role on the way the pore grows. The XRT observations were performed on solidified samples, and thus the regions of eutectic composition were assimilated to locations of the last liquid to solidify. However, unfortunately, the limited resolution of XRT did not allow for accurate curvature estimations on those locations. Calculating the curvature distribution all over the pores surface, Felberbaum *et al.* found that the majority of surface patches where the mean curvature, $H = 0.5(\kappa_1 + \kappa_2)$, is positive, are on the pore–eutectic interface (κ_1 and κ_2 are the two principal radii of curvature). Based on these findings, they assumed all surface patches with κ_1 and $\kappa_2 > 0$ to be on the pore–eutectic interface (*i.e.*, pore–liquid interface before the end of solidification). One example of an observed pore and its corresponding interfacial shape distribution* (ISD) plot,[11] considering only $\kappa_1 > 0$ and $\kappa_2 > 0$ values, is presented in Figure 1. A high density of surface patches can be observed close to the $\kappa_1 = 0$ line in areas where $\kappa_2 > 0$ (cylindrical pore morphology).

In fact, the pore–liquid interface should indeed have a positive mean curvature, but this does not require both κ_1 and κ_2 to be positive. On the other hand, on a solidified sample, not all surface patches where $\kappa_1 > 0$ and $\kappa_2 > 0$ can be attributed to a pore–liquid interface before the end of solidification is reached. During its growth, the pore can grow into cylindrical liquid channels that have non-eutectic composition thus leaving a pore with $\kappa_1 = 0$ and $\kappa_2 > 0$ before the eutectic temperature is reached. PhF simulations are performed in the current contribution to complement such experiments.

In the model, three PhF variables, $\phi_i(\mathbf{X}, t)$, where $i = s, l, p$ is a phase index, are introduced to show the distribution of the solid, liquid, and pore, respectively, in time and space. These variables can be understood as local volume fractions and thus linked together using the constraint. $\phi_s + \phi_l + \phi_p = 1$. A Lagrange multiplier, Λ, is introduced into the model in order to satisfy this constraint (Eq. [1]). The spatial and temporal

*ISD plots, first introduced by the group of Voorhees and coworkers is a two-dimensional probability contour plot, $P(\kappa_1, \kappa_2)$, which measures the probability of having a surface patch, with its principal curvatures falling in the range $[\kappa_1 - \Delta\kappa/2, \kappa_1 + \Delta\kappa/2]$ and $[\kappa_2 - \Delta\kappa/2, \kappa_2 + \Delta\kappa/2]$. $\Delta\kappa$ is the binning size used for calculating the ISD plot.

HOSSEIN MEIDANI, formerly Ph.D. Student with the Computational Materials Laboratory, Institute of Materials, Ecole Polytechnique Fédérale de Lausanne, 1015 Lausanne, Switzerland, is now Dev. Engineer with the Thermal Transverse Technologies (TTTM), Alstom (Switzerland), Brown Boveri Str. 7, 5401 Baden, Switzerland. Contact e-mail: h.meidani@gmail.com ALAIN JACOT, Senior Scientist, is with the Computational Materials Laboratory, Institute of Materials, Ecole Polytechnique Fédérale de Lausanne, and also with the Calcom ESI SA, Parc Scientifique, PSE-A, 1015 Lausanne, Switzerland. MICHEL RAPPAZ, Professor, is with the Computational Materials Laboratory, Institute of Materials, Ecole Polytechnique Fédérale de Lausanne.

Manuscript submitted April 14, 2014.
Article published online November 11, 2014

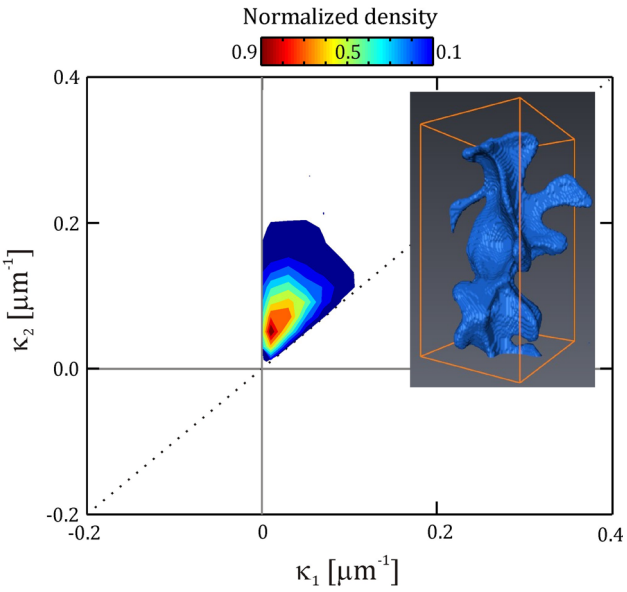

Fig. 1—ISD plot showing the curvature distribution on surface patches that satisfy the condition, $\kappa_1 > 0$ and $\kappa_2 > 0$. The inset shows the corresponding 3D reconstruction of the pore observed in XRT (from Ref. [10]) (Color figure online).

evolution of the PhF variable ϕ_i is given by the following partial differential equation[13]:

$$\dot{\phi}_i = \sum_{k \neq i} M_{ik} \begin{bmatrix} \varepsilon_{ik}^2 \left(\phi_k \nabla^2 \phi_i - \phi_i \nabla^2 \phi_k \right) \\ - 2W_{ik} \phi_k^2 (1 - \phi_k)^2 \phi_i (1 - \phi_i)(1 - 2\phi_i) \\ - 30 \phi_i \phi_k (1 - \phi_i)(1 - \phi_k) \Delta G_{ik} - \Lambda \end{bmatrix} \quad [1]$$

with

$$\Delta G_{\mathrm{sl}} = \Delta s_{\mathrm{f}} \Delta T \quad \Delta G_{\mathrm{lp}} = p_{\mathrm{p}} - p_{\mathrm{l}} \quad \Delta G_{\mathrm{sp}} = 0 \quad [2]$$

and

$$W_{ik} = \frac{15\sqrt{2}\gamma_{ik}}{\delta_{ik}} \quad \varepsilon_{ik}^2 = 2W_{ik}\delta_{ik}^2 \quad M_{ik} = \frac{\mu_{ik}}{\delta_{ik}}, \quad [3]$$

where Δs_{f} is the volumetric entropy of melting, ΔT is the undercooling, p_{p} and p_{l} are the pressures in the pore and in the liquid, respectively, ε_{ik}^2, M_{ik}, and W_{ik} are the three PhF parameters associated with the physical parameters γ_{ik}, μ_{ik}, and δ_{ik} describing the interfacial energy, the mobility, and the interface thickness, respectively, between phases i and k.[12]

Effect of the radius of the curvature of the pore is taken into account through the driving force term, for the liquid/pore transformation. It is expressed here as the pressure difference between the pore and the liquid, which can be justified by solving the steady-state form of Eq. [1] in spherical coordinates, for a single pore surrounded by the liquid. Doing so, the Laplace pressure condition is recovered:

$$p_{\mathrm{p}} - p_{\mathrm{l}} = 2\gamma_{\mathrm{lp}} H, \quad [4]$$

where H is the mean curvature of the pore–liquid interface.

Table I. Parameters Used for Phase-Field Calculations

Parameter	Unit	Numerical Value
Mesh size	μm	9.25×10^{-2}
δ_{ik}	μm	1.48
Domain size (x, y, z)	μm	$65.1 \times 116.9 \times 57.0$
p_{l}	Pa	10^5
T	K	1000
μ_{ls}	$\mathrm{m^3\ J^{-1}\ s^{-1}}$	1×10^{-6}
D_{l}	$\mathrm{m^2\ s^{-1}}$	1×10^{-6}
S_l	$\mathrm{mol_H\ m^{-3}}$	0.69
γ_{pl}	$\mathrm{J\ m^{-2}}$	0.9
γ_{ps}	$\mathrm{J\ m^{-2}}$	1.1
γ_{ls}	$\mathrm{J\ m^{-2}}$	0.2

Throughout this article, for the sake of simplicity, we will focus on aluminum alloys, where hydrogen is known to be the main gas responsible for pore formation.[10]

In this model, hydrogen diffusion in the liquid is assumed to govern the growth kinetics of the pore. This is taken into account in the model through a hydrogen conservation equation, neglecting any hydrogen concentration gradient in the gas phase and any hydrogen transport in the liquid due to convection. Sievert's law is also introduced to describe the chemical equilibrium and the pore is treated itself as a perfect gas.

The solidification and the effect of shrinkage are neglected in the model. More details on the model and validation tests can be found in References 13, 14.

A solid structure reconstructed from XRT observations of Felberbaum et al.[10] on an Al-4.4 wt pctCu specimen is used for the analysis (Figure 1). The region of interest includes a pore and its surrounding eutectics and primary phase. For the PhF calculation, only the primary solid phase is extracted from the image stacks, while the rest of the RVE, *i.e.*, eutectic phase and porosity, is assumed to be the interdendritic region available for the pore to advance in it.

For numerical reasons and for the current model to be accurate, the mesh spacing, ΔX, should be such that $\frac{r_{\mathrm{p}}^{\mathrm{c}}}{\Delta X} \geq 16$, where $r_{\mathrm{p}}^{\mathrm{c}}$ is the radius of curvature of the pore–liquid interface. Therefore, the extracted stack that had a size of $88 \times 158 \times 77$ voxels, in x, y, and z directions, respectively, was refined with voxels that were 8 times smaller using the ImageJ software.[15] This offers an additional advantage while trying to identify the pore–liquid interface and then calculating its curvature.

As an initial condition, a small pore was nucleated at the center of the domain and the interdendritic liquid was supersaturated in hydrogen, which corresponds to a driving force for the pore to grow. A zero-flux boundary condition is applied for hydrogen diffusion; therefore the number of moles of hydrogen in the domain stays constant while the pore evolves to reach its equilibrium state. In order to capture the pore morphology at different stages of its growth, the hydrogen concentration was increased step by step, each time letting the pore stabilize (reach equilibrium state). The initial concentration inside the domain was set to $c_{\mathrm{H}}^0 = 20\ \mathrm{mol_H\ m^{-3}}$ and was later increased to 50, 80,

100, and 120 $mol_H\ m^{-3}$. The other model parameters are given in Table I.

Variations of the pore size and its internal pressure are illustrated in Figure 2. The vertical dashed lines correspond to an increase of the hydrogen concentration, after the pore has reached an equilibrium state. The hydrogen concentration is increased inside the domain by multiplying all the concentration values by a constant. The sudden increase of the concentration inside the pore causes its pressure, which is calculated based on c_H^0 and using the prefect gas law, to increase instantaneously. For each c_H^0, as the pore grows, this pressure is relaxed with time and finally reaches equilibrium. The initial states of the pore, as well as its equilibrium state for each c_H^0, are illustrated in Figure 3. It can be observed that the simulated morphology of the pore for $c_H^0 = 100$ (Figure 3(c)), is very similar to that observed in the experiment (inset in Figure 1). Of course, the pore occupies gradually the volume that is allowed for its growth. However, the pore could potentially grow in various ways due to the complex shape of the volume of liquid available for its growth. The obtained pore morphology is the one satisfying the mechanical and thermodynamical equilibrium on all the small liquid–pore interfacial regions.

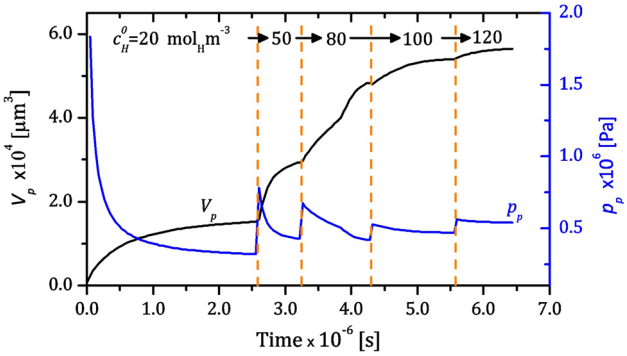

Fig. 2—The evolution of the pore volume and pressure with time. The hydrogen concentration is increased step by step each time letting the pore to stabilize. These c_H^0 increasing instants are indicated with vertical dashed lines (Color figure online).

For very high concentration values of 100 and 120 $mol_H\ m^{-3}$, the growth rate decreases as the pore reaches narrower and narrower channels located at the boundaries of the domain. Besides, as the pore grows, its equilibrium-state radius of curvature (which can be linked to its pressure) only changes slightly. This is in agreement with the findings in Reference 14, where the pore growth was simulated for simplified solid morphologies. It was found that the radius of curvature of the pore is bound between two limits, which depend on the statistical distribution of liquid channel widths.

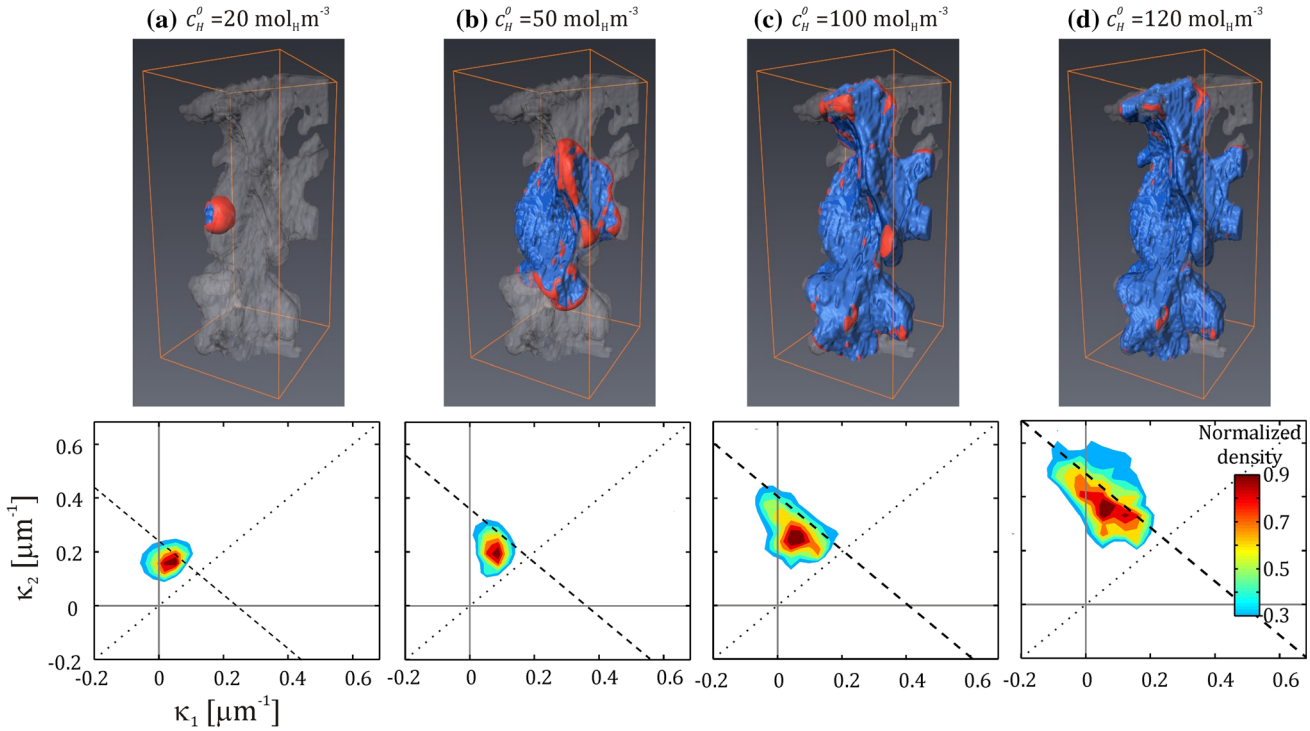

Fig. 3—3D reconstruction and ISD plots of the initial state of the pore (a) and its equilibrium morphologies for different hydrogen concentrations (b through d). The pore–liquid interface is colored in red and the pore–solid interface is in blue. The dashed line ($\frac{1}{2}(\kappa_1 + \kappa_2) = H = cte$) in the ISD plots represents the calculated mean curvature, H, obtained from the extracted ($p_p - p_l$) values from the phase-field calculations and using Laplace–Young's equation (Color figure online).

The morphology of the pore–liquid interface, in particular the corresponding ISD plot, was also studied at the various instants corresponding to the equilibrium states shown in Figure 3. To compute the ISD plots, a procedure similar to that used in Reference 14 was employed. The surface given by all the mesh points (similar to voxels in XRT) where $\phi_p = \phi_l = 0.5$ was extracted. Then, using the Avizo software, the surface was smoothened by triangular elements and, on each element, the principal curvatures were calculated. The dashed line on Figure 3 indicates the average mean curvature, calculated using the $(p_p - p_l)$ values extracted from the calculation and Laplace–Young's equation (Eq. [4]). For all plots, there is a generally good agreement between the curvature calculated from the shape of the simulated pore and the average mean curvature obtained from the pore pressure, although the local mean curvatures tend to be smaller. This discrepancy is due to the numerical difficulties to calculate the local curvature, which is a second derivative with respect to the PhF variables.

For the two lowest concentrations of 20 and 50 $mol_H\ m^{-3}$, the distribution is relatively narrow and circular. It is also quite close to the $\kappa_1 = \kappa_2$ line, which represents a spherical morphology. However, with further increase of the concentration, the distribution of curvature becomes elongated along the dashed line and toward the $\kappa_1 = 0$ region. In other words, while the mean curvature value is uniform on the pore–liquid interface, as the pore grows, it adapts a shape that features a higher fraction of cylindrical surface patches ($\kappa_1 = 0$ and $\kappa_2 > 0$) compared with spherical ones ($\kappa_1 = \kappa_2$). It can be observed that the PhF model can be used in order to better exploit experimental observations. Since, the XRT technique offers a limited spatial and temporal resolution, only general trends in the morphology of pores, and furthermore for as-solidified samples, could be observed so far.[10] The PhF model allows a better interpretation of the experiments by performing simulations with higher spatial and temporal resolutions, offering quantitative information about the growth of the pore, *i.e.*, its pressure and its curvature distribution. The pore morphology at different stages of its growth could also be studied with the model, which is currently not possible to achieve with the XRT technique.

The authors would like to thank the Swiss Competence Centre for Materials Science and Technology (CCMX) and partner companies, Asulab, Constellium, Kugler Bimetal, Novelis, Rolex and Varinor, within the thematic area "Multi-scale, multi-phenomena modeling of metallic systems" for funding this research.

REFERENCES

1. J.A. Dantzig and M. Rappaz: *Solidification*, 1st ed., EPFL Press, Lausanne, 2009.
2. A. Sabau and S. Viswanathan: *Metall. Mater. Trans. B*, 2002, vol. 33B, pp. 243–55.
3. C. Pequet, M. Rappaz, and M. Gremaud: *Metall. Mater. Trans. A*, 2002, vol. 33A, pp. 2095–106.
4. P.D. Lee and J.D. Hunt: *Conference on Modeling of Casting, Welding and Advanced Solidification Processes VII*, TMS, Warrendale, PA, 1995, p. 585.
5. R.C. Atwood, S. Sridhar, W. Zhang, and P.D. Lee: *Acta Mater.*, 2000, vol. 48, pp. 405–17.
6. K.D. Carlson, Z. Lin, and C. Beckermann: *Metall. Mater. Trans. A*, 2007, vol. 38A, pp. 541–55.
7. K. Kubo and R. Pehlke: *Metall. Trans. B*, 1985, vol. 16B, pp. 359–66.
8. G. Couturier and M. Rappaz: *Conference on Modeling of Casting, Welding and Advanced Solidification Processes*, TMS Publ., Warrendale, PA, 2006, p. 143.
9. D.R. Poirier, K. Yeum, and A.L. Maples: *Metall. Trans. A*, 1987, vol. 18A, pp. 1979–87.
10. M. Felberbaum and M. Rappaz: *Acta Mater.*, 2011, vol. 59, pp. 6849–60.
11. R. Mendoza, J. Alkemper, and P. Voorhees: *Metall. Mater. Trans. A*, 2003, vol. 34A, pp. 481–89.
12. W.J. Boettinger, J.A. Warren, C. Beckermann, and A. Karma: *Annu. Rev. Mater. Res.*, 2003, vol. 32, pp. 163–94.
13. H. Meidani and A. Jacot: *Acta Mater.*, 2011, vol. 59, pp. 3032–40.
14. H. Meidani, J.L. Desbiolles, A. Jacot, and M. Rappaz: *Acta Mater.*, 2012, vol. 60, pp. 2518–27.
15. C.A. Schneider, W.S. Rasband, and K.W. Eliceiri: *Nat. Methods*, 2012, vol. 9, pp. 671–75.